Available online at www.sciencedirect.com
ScienceDirect
C. R. Physique 8 (2007) 312–322
COMPTES RENDUS PHYSIQUE
http://france.elsevier.com/direct/COMREN/

Optical techniques for direct imaging of exoplanets/Techniques optiques pour l'imagerie directe des exoplanètes

Shaped pupil coronagraphy

N. Jeremy Kasdin [a,*], Robert J. Vanderbei [b], Ruslan Belikov [a]

[a] *Mechanical and Aerospace Engineering, Princeton University, Princeton, NJ 08544, USA*
[b] *Operations Research and Financial Engineering, Princeton University, Princeton, NJ 08544, USA*

Available online 5 June 2007

Abstract

At Princeton we have been studying shaped pupil coronagraphs for high contrast imaging and planet finding. These will find applications in both ground and space imaging. In this article we summarize the design procedure for shaped pupils and review the various families of designs we have found. We describe the manufacturing processes we have used to make free standing shaped pupil masks and review our most recent laboratory results with and without wavefront control. We also discuss the factors limiting high contrast in the laboratory and our plans for mitigating them. ***To cite this article: N.J. Kasdin et al., C. R. Physique 8 (2007).***

Résumé

Coronographie à pupille binaires. Notre groupe à Princeton se focalise sur l'étude de coronographes à pupille binaires dans le contexte de l'imagerie à très haut contraste et de la détection d'exo-planètes. Nous étudions en parallèle leur application à des projets spatiaux et à des telescopes conventionnels. Dans cet article, nous introduisons la théorie nécessaire à la conception de tels masques, puis passons en revue différentes familles de diaphragmes capables de produire un contraste de 10 ordres de grandeur. Nous décrivons ensuite la fabrication de ces pupilles binaires et nous présentons nos validations expérimentales, avec et sans controle de front d'onde. Nous discutons les facteurs limitant le contraste au sein de notre banc d'essai et nos projets pour les éliminer. ***Pour citer cet article : N.J. Kasdin et al., C. R. Physique 8 (2007).***

Keywords: Coronagraphy; Apodization; Shaped pupil; High contrast imaging

Mots-clés : Coronographie ; Apodisation ; Pupillle binaires ; Imagerie à fort contraste

1. Introduction

The first discovery of Jupiter-sized exoplanets more than 10 years ago and the subsequent discovery that such planets are fairly common have inspired the search for smaller, more Earth-like, planets. The indirect methods used to date for planet discovery are constantly being improved in the sense that smaller-mass planets at greater distances from their host star are being discovered. With their current and projected capabilities, however, these methods are ill-suited for detecting Earth-mass planets at separations of 1 AU from Sun-like stars. For such discoveries, direct observation seems to be a more promising approach. However, even this is extraordinarily challenging when one

* Corresponding author.
E-mail addresses: jkasdin@princeton.edu (N.J. Kasdin), rvdb@princeton.edu (R.J. Vanderbei), rbelikov@princeton.edu (R. Belikov).

1631-0705/$ – see front matter
doi:10.1016/j.crhy.2007.02.009

considers that (i) such a planet can be expected to be only 10^{-10} times as bright as its host star, (ii) the separation at greatest elongation can be expected to be on the order of 0.1 arcseconds, and (iii) the exo-zodiacal light may outshine the planet.

Over the past five years or so, there have been several design architectures proposed for direct imaging of exoplanets. Most of these designs are for space-based telescopes, as the atmospheric disturbance for ground-based instruments poses what seems an insurmountable problem for detecting Earth-like planets (although larger ones might be imageable from the ground). The space-based design concepts include infrared nulling interferometers, improved versions of a traditional Lyot coronagraph, an external occulter positioned tens of thousands of kilometers in front of a large-aperture but otherwise simple telescope, a conventional off-axis large-aperture telescope employing a custom-shaped (or apodized) entrance pupil to control the ideal diffraction pattern, and others.

While we have participated in several of these design concept studies, we have been at the forefront of the research into shaped pupil designs. The purpose of this article is to summarize the main ideas and present some of the best high-contrast shaped pupils we have developed to date. Also, the shaped pupil only achieves high contrast if the wavefront is of sufficient (exquisite!) quality. Hence, this design is intimately connected with wavefront control schemes. In this paper, we also review our work on wavefront control and we describe our laboratory experiments where we are making steady progress toward achieving 10^{-10} contrast.

2. Shaped pupil families

In order to discuss pupil apodized telescopes, we begin with the Fraunhoffer integral, which relates the on-axis unaberrated pupil-plane electric field, after an apodization given by $\mathcal{A}(x, y)$, to the electric field at an image plane,

$$E(\xi, \zeta) = \iint_S \mathrm{e}^{-2\pi \mathrm{i}(x\xi + y\zeta)} \mathcal{A}(x, y)\, \mathrm{d}x\, \mathrm{d}y \tag{1}$$

where S denotes the pupil aperture (which can be of any shape). Note that here we have chosen to use dimensionless coordinates, so that (x, y) represent rectangular coordinates in the pupil in units of aperture diameter, D, and (ξ, ζ) are angular measures in Cartesian directions in the image in units of λ/D radians. The *point-spread function* (*PSF*) is the square of the magnitude of the image-plane electric field.

The general problem of finding an arbitrary apodization can be rather complicated. However, there are two special cases that simplify the problem and are of interest to us here. The first is where the apodization can be written in 'product form' $\mathcal{A}(x, y) = A_1(x)A_2(y)$, which yields an electric fields that also has a product form $E(\xi, \zeta) = E_1(\xi)E_2(\zeta)$,

$$E(\xi, \zeta) = \int_{-1/2}^{1/2} A_1(x)\mathrm{e}^{-2\pi \mathrm{i} x\xi}\, \mathrm{d}x \int_{-1/2}^{1/2} A_2(y)\mathrm{e}^{-2\pi y\zeta}\, \mathrm{d}y \tag{2}$$

where we are taking S to be a square aperture. Hence, if we can find an apodization in one direction, say the x direction, that achieves high contrast, then that high contrast automatically extends in the other (y) direction. In fact, one could apodize separately in both directions creating extremely high contrast along the diagonal (Nisenson and Papaliolios [1]).

In the case where the apodization function is circularly symmetric, i.e., $\mathcal{A}(x, y) = \mathcal{A}(r)$, where $r = \sqrt{x^2 + y^2}$, it is convenient to rewrite the Fraunhoffer integral using polar coordinates. The electric field in the image plane then becomes the one-dimensional Hankel transform of the apodization,

$$E(\rho) = \int_0^{1/2} \int_0^{2\pi} \mathrm{e}^{-2\pi \mathrm{i} r\rho \cos(\theta - \phi)} \mathcal{A}(r) r\, \mathrm{d}\theta\, \mathrm{d}r = 2\pi \int_0^{1/2} J_0(2\pi r\rho)\mathcal{A}(r) r\, \mathrm{d}r \tag{3}$$

The high-contrast apodization problem is easy to state: find an apodization function, $\mathcal{A}$, that gives a point spread function with the desired light suppression (i.e., contrast) at angles favorable to planet detection (i.e., small angles). Surprisingly, this problem was solved quite beautifully in the early 1960s. In 1965, Slepian [2] showed that the prolate spheroidal wavefunction is the optimal high-contrast apodization in a single direction for the rectangular, product

form in Eq. (2). For the circularly symmetric case, he developed the generalized prolate spheroidal wavefunction as an optimal solution to the finite Hankel transform for circular telescopes given in Eq. (3). This solution has the advantage of a full 360 degree discovery space but at the cost of lower telescope throughput. This classical pupil apodization is an elegant and simple approach to achieving a high-contrast point spread function suitable for planet finding. Unfortunately, it is extremely difficult to manufacture the attenuating pupil masks to the accuracy needed for planet finding, and to make them behave the same over a broad band of wavelengths.

Our solution to the manufacturing problem is to restrict ourselves to binary apodization functions, that is, ones where the apodization function $\mathcal{A}(x, y)$ takes on only the values zero or one. We call these *shaped pupils* as they are equivalent to modifying the entrance aperture shape of the telescope. Shaped pupils are far easier to manufacture than classically apodized ones as they only involve cutting the proper openings in a mask. They are also fundamentally polychromatic; a given shaped pupil coronagraph operates identically at all wavelengths. Our first shaped-pupil design consisted of an opening of the form $\{(x, y)\colon |y| \leqslant a(x)\}$. For this shape, the image-plane electric field on the $\zeta = 0$ axis is given by,

$$E(\xi, 0) = \int_0^{1/2} a(x) \cos(2\pi \xi x)\, \mathrm{d}x$$

This is identical to one of the directions in Eq. (2); the best shape is therefore given by the prolate spheroidal wavefunction (Kasdin et al. [3]). This pupil and it's corresponding point spread function are shown in Fig. 1.

While this shaped pupil does reach the desired contrast of 10^{-10}, it does so only in a very narrow wedge of the image plane. It is desirable, therefore, to find shaped pupils that widen this region of high contrast, while retaining the advantages of the approach. If we still consider pupils in rectangular openings with shapes of the product form in Eq. (2), we can formulate the one-dimensional apodization problem as follows:

$$\begin{aligned} &\text{maximize} \int_0^{1/2} A_1(x)\, \mathrm{d}x \\ &\text{subject to } -10^{-5} E_1(0) \leqslant E_1(\xi) \leqslant 10^{-5} E_1(0), \quad \xi_{\mathrm{iwa}} \leqslant \xi \leqslant \xi_{\mathrm{owa}} \\ &\qquad 0 \leqslant A_1(x) \leqslant 1, \quad 0 \leqslant x \leqslant 1/2 \end{aligned} \tag{4}$$

where

$$E_1(\xi) = \int_0^{1/2} \cos(2\pi x \xi) A_1(x)\, \mathrm{d}x$$

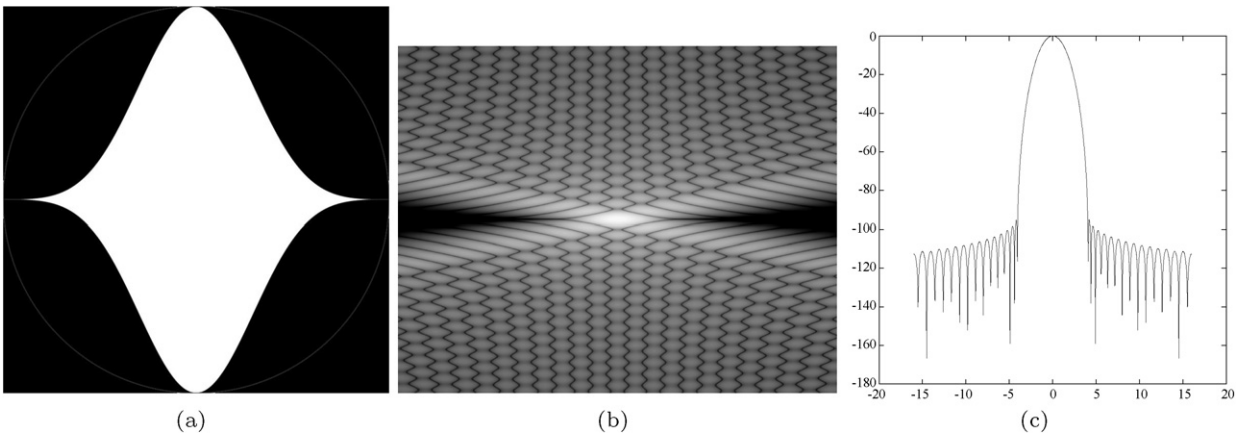

Fig. 1. (a) The Spergel–Kasdin prolate-spheroidal mask. (b) The associated 2-D point spread function and (c) its ξ-axis slice shown in decibels ($10^{-10} = -100$ dB).

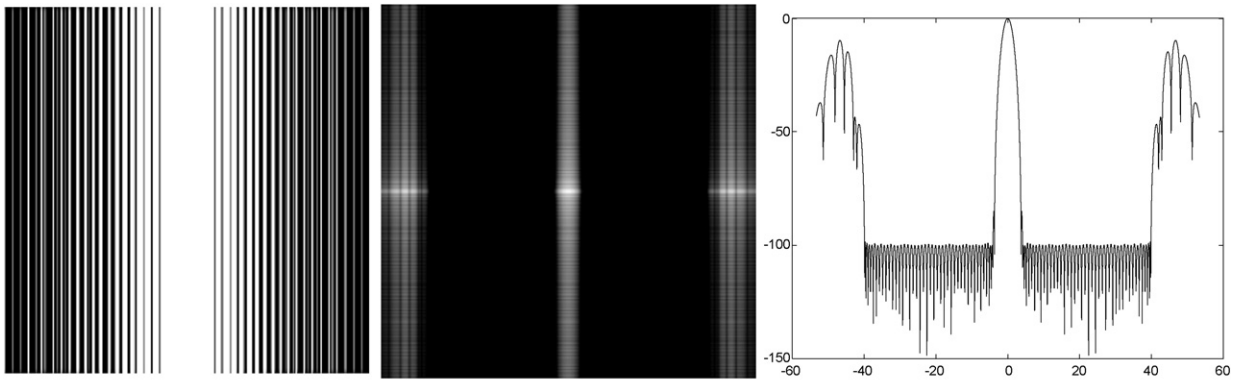

Fig. 2. (a) A barcode mask. (b) The corresponding psf. (c) A cross-section of the psf. This pupil has an iwa of 4 λ/D and throughput (more precisely, Airy throughput—see [6]) of 25%.

This is a linear programming problem and is thus quickly and easily solved numerically. The numerical solution of this problem turns out to be zero-one valued; the optimal solution is a shaped pupil. We call the resulting mask a *barcode mask*. The specific edge locations of each slot are found by solving a similar optimization problem, using the above solution as a starting guess, where the electric field in the image plane is now given by,

$$E(\xi) = \sum_{i=1}^{m} \frac{1}{\pi\xi}\big(\sin(2\pi\xi x_{i+1}) - \sin(2\pi\xi x_i)\big) \tag{5}$$

where the x_i represent the edge location of each slot in the mask. This is a more difficult optimization as the contrast constraint is now non-linear in the optimization variables, making the problem both nonlinear and nonconvex. We solve it using Vanderbei's LOQO optimizer (Vanderbei [4]). An example of a barcode mask with its corresponding point spread function is given in Fig. 2. In Vanderbei et al. [5] we describe another class of rectangular masks that consist of the tensor product of two barcode masks rotated by 90 degrees. These have the advantage of producing a much smaller inner working angle along the diagonals while achieving the same contrast, though at the expense of a loss in throughput.

A second class of rectangular shaped pupils consists of multiple openings similar to the single pupil in Fig. 1. The shape of each edge is found via a similar optimization as for the barcode (i.e., maximizing a surrogate of throughput subject to a contrast constraint). Assuming the openings are symmetric about the center of the pupil, the electric field in the image plane is now given by the expression,

$$E(\xi,\zeta) = \frac{2}{\pi}\int_0^{1/2}\sum_{n=0}^{N-1}\cos(2\pi x\xi)\frac{\sin(2\pi\zeta t_n(x)) - \sin(2\pi\zeta b_n(x))}{\zeta}\,\mathrm{d}x \tag{6}$$

where $b_n(x)$ is the bottom edge of opening n and $t_n(x)$ is the top edge of opening n. We now use our numerical tools to directly find these shapes over a set of points by optimizing the open area of the pupil. We also set the sector of the image plane where the contrast is constrained (that is, the discovery space). We call these masks *ripple masks*. Two examples of such masks are shown in Fig. 3. The first mask, *ripple 1*, is inscribed in an ellipse since it was designed for a Terrestrial Planet Finder design that included an elliptical primary mirror, chosen to provide the highest resolution possible while remaining within the constraints of the launch vehicle size. The second mask, *ripple 3*, is inscribed in a circle and designed to fit into the High Contrast Imaging Testbed (HCIT) at the Jet Propulsion Laboratory. We also have ripple masks designs inscribed in circles and squares with varying inner working angles, discovery spaces, contrast, and throughput. More details on these, and other families of multi-opening, masks can be found in Kasdin et al. [3,6].

Finally, we have computed two additional families of masks using the polar form of the point spread function (Eq. (3)). These are circularly symmetric masks that allow for discovery in a full 360 degrees around the star. The first class is suggested by the barcode mask. Performing a similar optimization for a radial apodization as we did for the

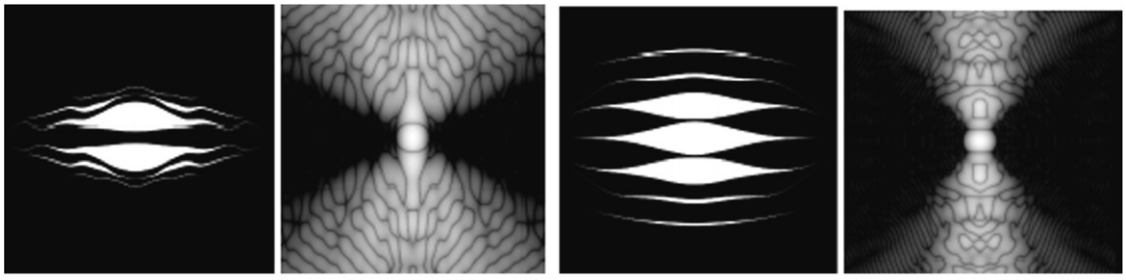

Fig. 3. Two directly optimized *ripple masks*, designed to open up the high-contrast region, and their corresponding psfs. (a) The 6 opening ripple 1 embedded in an elliptical pupil. (b) The corresponding PSF. Contrast of 10^{-10} extends over $\rho \geqslant 4$ in a 45 degree wedge. (c) The 7 opening ripple 3 embedded in a circular pupil. (d) The corresponding PSF. Contrast of 10^{-10} extends over $\rho \geqslant 4$ in a 90 degree wedge.

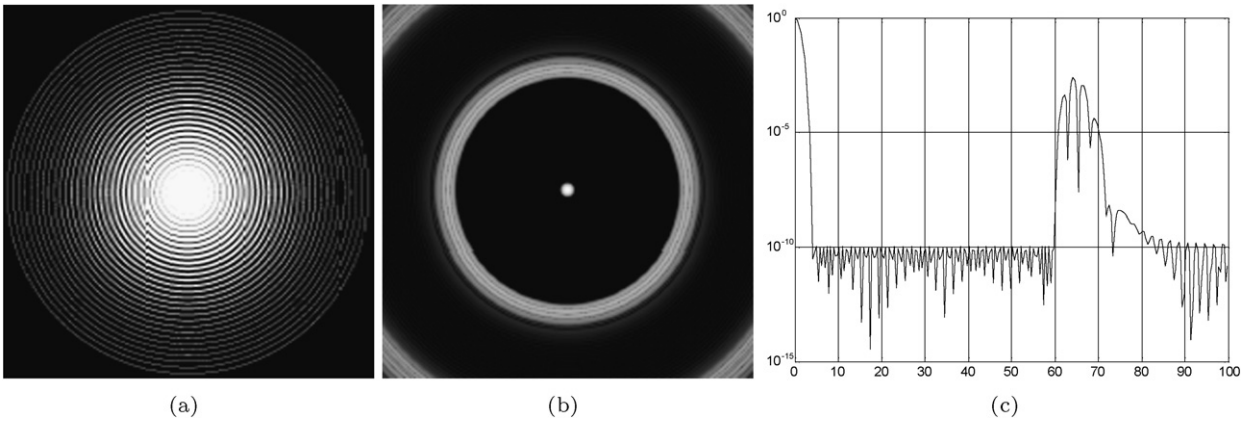

Fig. 4. (a) A concentric ring shaped pupil mask. (b) The corresponding psf. (c) A cross-section of the psf. This pupil has an iwa of 4 λ/D and an Airy throughput of 9%.

linear one above also results in a one-zero solution. We call the resulting mask a *concentric ring* mask. The electric field in the image plane for such a mask is given by the sum,

$$E(\rho) = \frac{1}{\rho}\sum_{k=0}^{m-1}\big(r_{2k+1}J_1(2\pi r_{2k+1}\rho) - r_{2k}J_1(2\pi r_{2k}\rho)\big) \tag{7}$$

where m is the number of open rings. We again use LOQO to find the optimal edge radii. An example of a concentric ring mask is shown in Fig. 4.

While concentric ring masks provide a wider discovery space (though with lower throughput than ripple masks), they cannot be manufactured as free standing masks; they must be layed on glass, which raises concerns of ghost images and other aberrations. One solution is to introduce radial spiders to support the rings. In Vanderbei et al. [7] we show how such spiders can be designed without any degradation to the point spread function (not surprisingly, we call these *spiderweb masks*).

For our second class of circularly symmetric masks we eliminate the concentric rings and use only the spiders. By carefully choosing the shape of the spiders we can approximate any radial apodization and reproduce the point spread function within some range of ρ. If $\alpha(r)$ is the shape, in azimuth, of each spider, then the electric field at the image is given by,

$$E(\rho,\phi) = \int_0^{1/2} J_0(-2\pi r\rho)\big(2\pi - N\alpha(r)\big)r\,\mathrm{d}r - \sum_{j\neq 0}\int_0^{1/2} i^{jN}J_{jN}(-2\pi r\rho)\mathrm{e}^{-jN\phi}\frac{2}{j}\sin\left(jN\frac{\alpha(r)}{2}\right)r\,\mathrm{d}r \tag{8}$$

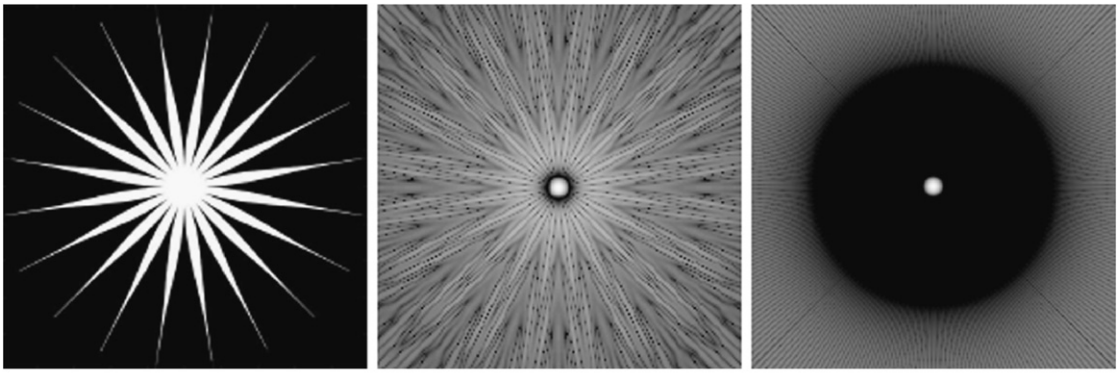

Fig. 5. (a) A starshaped pupil mask with 20 rays. (b) The corresponding psf. (c) The psf of the starshaped mask with 150 rays.

where N is the number of rays. We show in Vanderbei et al. [8] that the second term in this expression can be made arbitrarily small by selecting N large enough. We also show that by selecting,

$$\alpha(r) = \frac{2\pi}{N}\big(1 - A(r)\big) \tag{9}$$

the first term can be made to match any circularly symmetric apodization. We call the resulting masks *starshaped masks* since the designs resemble many-pointed stars. A sample starshaped mask reproducing a prolate spheroidal apodization is shown in Fig. 5 with $N = 20$ and $N = 150$ rays.

3. Manufacturing

Our first laboratory test sample was of the ripple 1 elliptical, multi-opening design (Kasdin et al. [6,3]). An image of the mask is shown in Fig. 6 (*left*). The test mask was manufactured at the National Institute of Standards and Technology in Boulder, CO using a deep reactive ion etching process on single crystal Si. The test mask is 1 inch across in its longest dimension, the size determined by a combination of the optics in the test setup, the wafer size, the fixturing, and the tolerancing. Si was chosen because of its excellent thermal properties, because it allows for extremely precise edge features, and because it is readily available. The availability of various processes for etching and coating Si also make this an attractive material. This particular mask was fabricated from a 76 mm diameter double-sided polished silicon wafer (320 micrometers thick, 1–10 ohm cm, p type, B doped, ⟨1–0–0⟩ oriented). The elliptical mask pattern was formed by double-sided deep reactive ion etching (DRIE) through the wafer. This process used alternating etch and edge passivation steps to allow high-rate silicon etching with vertical sidewalls. The first etch thins the regions around the mask holes to 50 μm, after which the wafer is flipped and the second etch cuts out the actual holes in the thinned areas. This is done to minimize the light interaction with the walls of the mask.

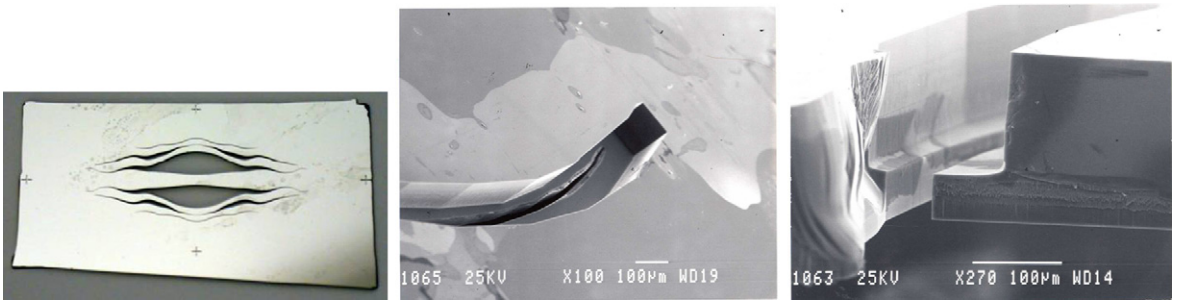

Fig. 6. Microscope images of our laboratory mask. The mask was made via deep ion etching of a 250 micron Si wafer, thinned to 50 microns near the openings. Feature accuracy is better than 10 microns.

Fig. 6 also shows scanning electron microscope images of the final mask used for testing. Edge accuracy is better than 10 microns.

Recently, the Jet Propulsion Laboratory (JPL) has duplicated this process, thus providing a second facility with the capability to make shaped pupil masks. There are small differences in the specifics of the process between NIST and JPL, such as the wafer used, durations of etches, etc., but the overall procedure is very similar. More details can be found in Balasubramanian et al. [9]. In addition to this process, JPL has developed a new process using silicon-on-oxide (SOI) wafers. These wafers provide a more controlled etch, resulting in improved edge characteristics and the possibility for certain desirable features, such as tapered side walls.

The shaped pupil theory described in the previous section assumes infinitely thin, perfectly conducting masks. It is therefore natural to ask whether the real three-dimensional masks being manufactured will perform as designed, achieving the desired 10^{10} contrast, given that light is an electromagnetic vector field that can interact with the structure of a mask in a complex manner. Fortunately, for most cases of interest, these assumptions are indeed valid. Ceperley et al. [10] have performed finite-difference-time-domain simulations of the interactions between the vector electromagnetic fields and the edges of a realistic mask, and Lieber et al. [11] have used those results to study the effects on the final contrast. Both studies concluded that any corrupting field effects are below the desired level provided that the mask has tapered rathered than perpendicular edges. For instance, for a 20 degree undercut, the difference between the scalar field theory and the exact, numerically propagated field was negligible. For masks that are not undercut, the degradation in contrast depends upon the mask type and size. For example, in a 10 cm-diameter, 50 μm-thick ripple 1 mask, contrast is degraded to 10^9, while for a 10 cm checkerboard mask, contrast is not degraded at all. The masks made so far are of the ripple type, are not undercut, and the sidewalls are all approximately 50 μm wide, so they will not achieve 10^{10} contrast level (without appropriate wavefront control). While plans call for experimenting with undercut masks in the near future, expectations are that any residual error due to vector field effects can be mitigated by the wavefront control system.

4. Laboratory results

For the past three years we have been developing a laboratory facility at Princeton for testing shaped pupil coronagraphs. The lab is comprised of two rooms that function as a pre-entry security area and high contrast imaging dark lab, respectively. Our lab consists of a 1.2 × 5 m vibration-isolated optical bench with an enclosure to eliminate thermal convection, particulate contamination, and stray light. We also use HEPA filters to further reduce particulate contamination and an AC system to stabilize the temperature and humidity. The optical bench setup is shown in Fig. 7. The purpose of the setup is to create a point source of light (artificial star), take its image with a coronagraph, and measure the contrast achieved in the dark zones of the PSF. The point source is created by coupling one of several sources into a fiber: a 532 nm laser pointer head; 2 He–Ne lasers at 594 nm (2 mW), and 632 nm (5 mW) respectively; and a Tungsten lamp white light source with color temperature of 3200 K. The diverging Gaussian beam from the fiber first goes through an aperture, gets collimated by an off-axis parabola, redirected by the deformable mirror, and

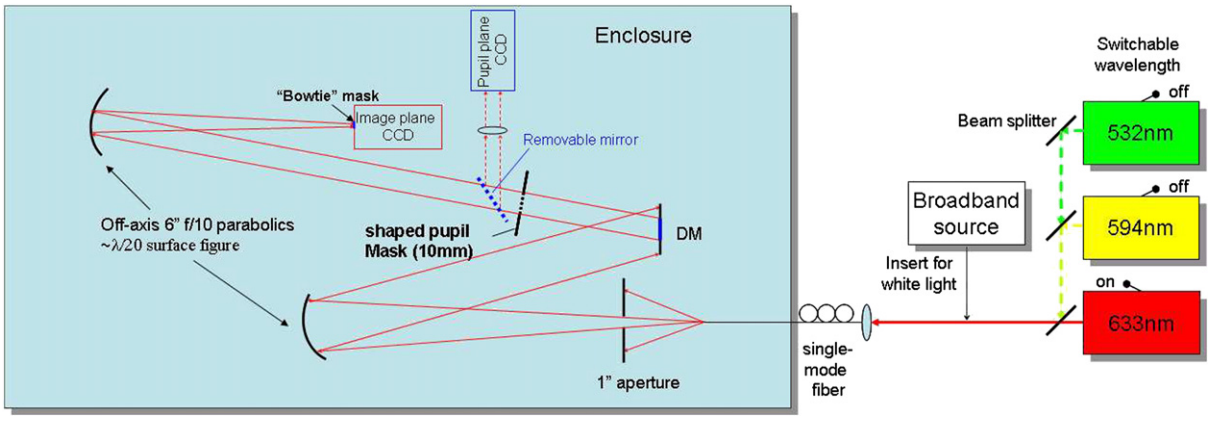

Fig. 7. Princeton laboratory schematic.

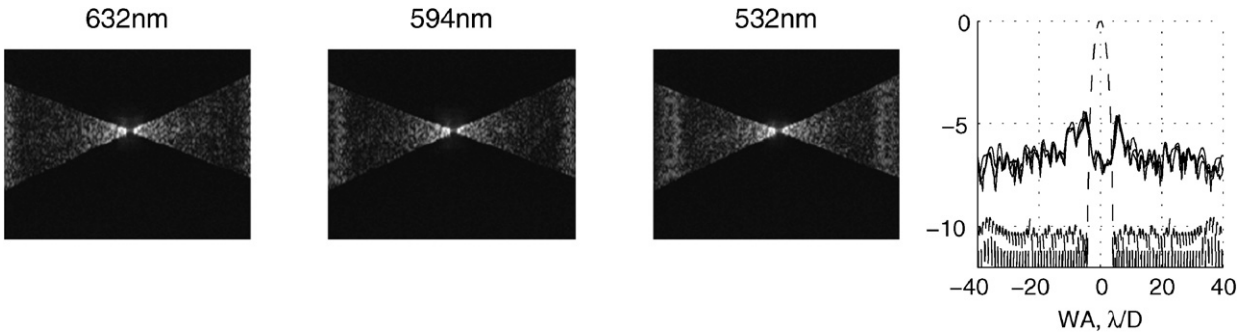

Fig. 8. Measurements at 3 different wavelengths. Right: superimposed slices for the three measurements (dashed line is the ideal PSF). For all three wavelengths, contrast is limited to roughly 10^{-5} at 4 λ/D.

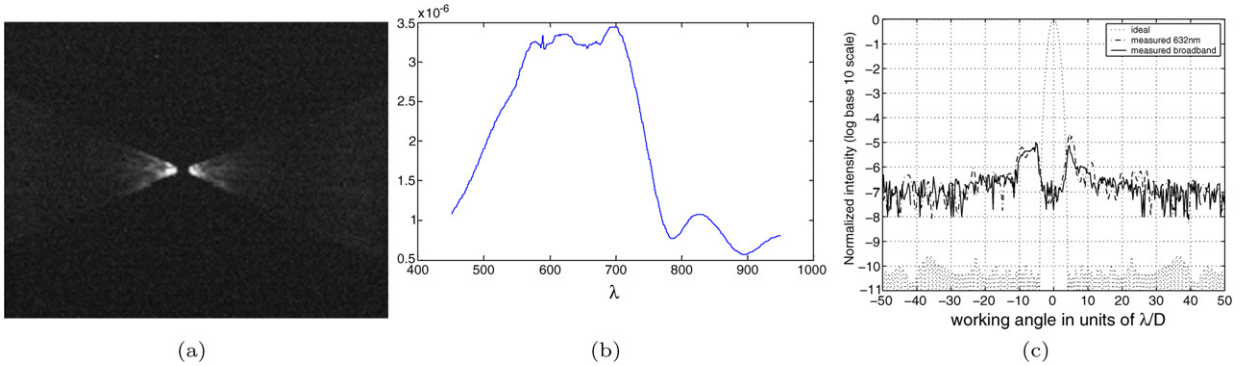

Fig. 9. (a) CCD image in white light (1 hour exposure); (b) Measured spectrum before the fiber; (c) Slice through the CCD image.

finally illuminates the shaped pupil. The beam illuminating the shaped pupil has approximately a flat wavefront and a uniform amplitude profile, but with some phase and amplitude aberrations, as it would in a real telescope. The beam goes through the shaped pupil, and is focused onto a cooled CCD by a second off-axis parabola. The CCD, which is the equivalent of the science camera, records the PSF. Fig. 8 shows a sample measurement in three wavelengths using the 1 inch diameter elliptical ripple 3 mask manufactured by NIST (shown in Fig. 6). On these images, the bright portions of the PSF have been blocked by an image plane mask placed on the surface of the CCD. This mask, which we call 'bowtie', blocks the bright portions of the PSF and admits only the dark zones. Without the bowtie, blooming and other artifacts drown the actual signal in the dark zone.

In Fig. 9, we present the results of our measurements in broadband light. Included in the figure is the spectrum of our light source, which extends from approximately 550 to 750 nm.

Both Fig. 8 and Fig. 9 show the CCD images and contrast measurements prior to wavefront control. For these experiments we used a flat $\lambda/20$ mirror in place of the DM. It is clear from the images in Fig. 8 that the dark zone of the PSF has been corrupted by scattered light. This halo, commonly referred to as 'speckles', results from wavefront aberrations induced by amplitude and phase errors in the optics. The brightest of these speckles is about 3×10^{-5} and located at roughly 4 λ/D, for all wavelengths.

A careful examination of the CCD images in Fig. 8 reveals that the PSF dilates with wavelength as expected. The graph on the right of Fig. 8 shows superimposed horizontal slices through the centers of the 3 images out to 40 λ/D. These traces have been stretched along the abscissa to reverse the dilation due to wavelength so that all are plotted on the same λ/D scale, thus corresponding to sky angle (or 'working angle'). Two things on this graph are noteworthy. First, the contrast is the same for different wavelengths, showing the achromaticity of shaped pupils at least at this contrast level. Second, the speckle structure itself looks very similar for different wavelengths, especially for the lower working angles, showing that our speckles are achromatic (that is, after known wavelength dependencies, such as dilation and multiplicative factors, are taken out). Therefore, they are most likely due to phase aberrations. Hence,

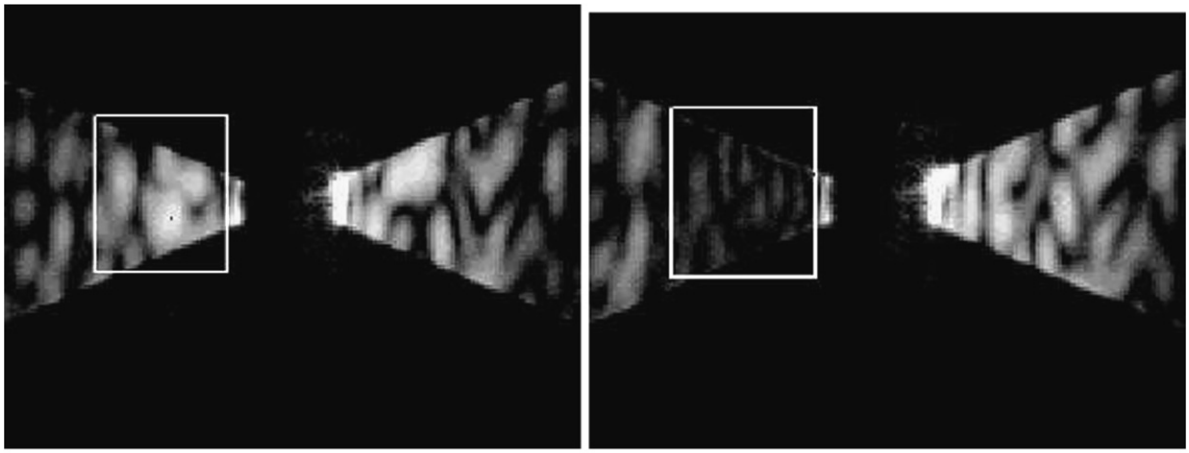

(a) (b)

Fig. 10. Classical Speckle Nulling on the Princeton Testbed. The control region extends from 5 to 12 λ/D and is shown by a white rectangle. (a) Before correction. Average contrast is 10^{-5} in the control region. (b) After correction. Average contrast is 10^{-6} in the control region.

techniques such as spectral differential imaging can be applied to improve contrast even further, but such studies are outside the scope of this article. We expect that after correcting for phase, and improving contrast, the speckle will begin to be dominated by amplitude error in the optics and thus show a different wavelength dependence.

In Fig. 9 the speckle image appears noisy due to the very low power of the white light source relative to the monochromatic ones. This is primarily due to the inherent inefficiencies in coupling a spatially incoherent light source into a single mode fiber. Because of this, electronic noise limits the measurements of contrast to approximately 4×10^{-7}. Nonetheless, it is still clear from Fig. 9 that the contrast in broadband light remains the same as in monochromatic light and that even the speckle structure is very similar, at least for low inner working angles. This once again demonstrates the broadband capabilities of shaped pupils.

Fig. 10 shows the first attempts at wavefront correction in the Princeton laboratory. For these, we used a smaller, circular shaped pupil (a 10 mm diameter ripple 3 made by JPL) to match the size of our 10 mm 32×32 Boston Micromachines MEMS deformable mirror (DM). The results shown are in 632 nm light, but the performance is essentially identical for other wavelengths as well. The correction scheme we employed is a minor modification of the classical speckle nulling algorithm as described in Belikov et al. [12]. (The original algorithm is due to Trauger and Burrows—see [13]). This algorithm corrects for both amplitude and phase error, monochromatically, on one side of the point spread function. The average contrast before actuating the DM was approximately 10^{-5} between 4 and 12 λ/D; after correction it improved to 10^{-6}. Both the speckles and the DM are very stable: one can turn the DM off, come back the next day, set the DM to the previous setting, and the dark hole reappears.

In addition to our Princeton testbed, we also have occasional access to JPL's High Contrast Imaging Testbed (HCIT) described in Trauger et al. [13]. The HCIT is more stable and with lower noise than the facility at Princeton. The optical bench is contained in a vibration isolated and thermally controlled vacuum chamber. The HCIT also contains a larger (30 mm) and more precise, DM. In this facility we were able to improve our corrected contrast by almost two orders of magnitude. Fig. 11 shows the results of our experiments with classical speckle nulling at the HCIT at 785 nm, 836 nm, and in broadband light. Without any corrections, the contrast on the HCIT testbed is similar to the Princeton testbed, i.e., 10^{-5} at 4 λ/D. After wavefront correction, the contrast was 4×10^{-8} between 4 and 9 λ/D (averaged across the dark region). As can be seen in Fig. 11, this contrast is maintained after switching to either 836 nm or broadband light, once again demonstrating achromaticity of shaped pupils. Furthermore, both the speckle pattern and the DM are stable, so that the dark hole reappears if the facility is shut off for periods of a day or more and then the DM is reset to the previously computed setting.

Simulations show that the contrast-limiting factor is the inability of the classical speckle nulling algorithm to correct speckles caused by certain manufacturing errors in the shaped pupil. This is believed to be the limitation both on the Princeton testbed as well as HCIT. We are currently manufacturing shaped pupils designed to avoid these

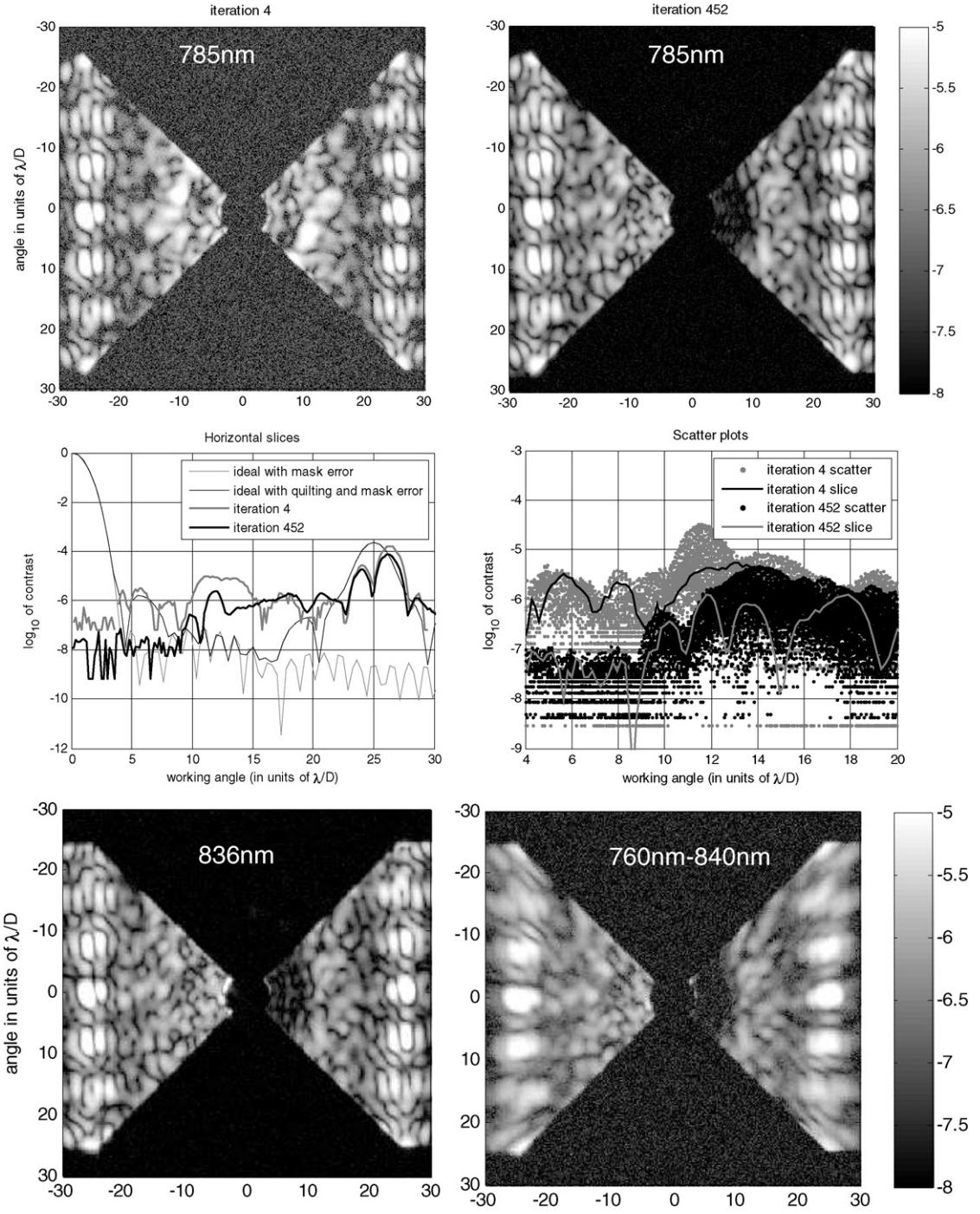

Fig. 11. Contrast plots from tests at the HCIT. Top left: one of the starting speckle nulling iterations (iteration 4) at 785 nm. Top right: one of the final iterations (iteration 452). The higher amount of noise in the image of iteration 4 is due to lower exposure time. Middle left: horizontal traces through the centers. Middle right: scatter plots in the dark region. Bottom left: after changing from 785 to 836 nm light. Bottom right: after changing to broadband light. For the λ/D scale, $\lambda = 785$ nm and $D = 25$ mm.

manufacturing errors, and are concurrently testing algorithms that are more sophisticated than classical speckle nulling and are not hindered by manufacturing error in shaped pupils. Our simulations indicate that the desired contrast of 10^{-10} is achievable with these modifications.

5. Final remarks

The effort to find and characterize Earthlike planets is intensely compelling to both scientists and the layman alike. The recent discoveries of planets as small as 7 Earth masses provide tantalizing hints of what we may find when we perfect the ability to image terrestrial planets in the habitable zone of their parent star. Shaped pupils are one of the handful of technologies being studied as potentially enabling a space based coronagraph for very high-contrast imaging. They provide many potential advantages over competing approaches, not the least of which being their simplicity, robustness, and achromaticity. In this article we have shown the great progress being made in the design and test of shaped pupil coronagraphs. We have developed a manufacturing process of flight quality and we have achieved contrasts of close to 10^{-8} in multiple wavelengths. Work continues on new designs, improved manufacturing approaches, and more efficient control algorithms, the ultimate goal being to achieve, in the laboratory, 10^{-10} contrast in broadband.

References

[1] P. Nisenson, C. Papaliolios, Detection of earth-like planets using apodized telescopes, The Astrophysical Journal 548 (2) (2001) L201–L205.
[2] D. Slepian, Analytic solution of two apodization problems, Journal of the Optical Society of America 55 (9) (1965) 1110–1115.
[3] N.J. Kasdin, R.J. Vanderbei, M.G. Littman, D.N. Spergel, Optimal one-dimensional apodizations and shaped pupils for planet finding coronagraphy, Applied Optics 44 (7) (2005) 1117–1128.
[4] R.J. Vanderbei, LOQO user's manual—version 3.10, Optimization Methods and Software 12 (1999) 485–514.
[5] R.J. Vanderbei, N.J. Kasdin, D.N. Spergel, Rectangular-mask coronagraphs for high-contrast imaging, Astrophysical Journal 615 (November 1, 2004).
[6] N.J. Kasdin, R.J. Vanderbei, D.N. Spergel, M.G. Littman, Extrasolar planet finding via optimal apodized-pupil and shaped-pupil coronagraphs, The Astrophysical Journal 582 (January 2003) 1147–1161.
[7] R.J. Vanderbei, D.N. Spergel, N.J. Kasdin, Spiderweb masks for high contrast imaging, Astrophysical Journal 590 (June 10, 2003) 593–603.
[8] R.J. Vanderbei, D.N. Spergel, N.J. Kasdin, Circularly symmetric apodization via starshaped masks, Astrophysical Journal 599 (1) (December 10, 2003) 686–694.
[9] K. Balasubramanian, P.M. Echternach, M.R. Dickie, R.E. Muller, V.E. White, D.J. Hoppe, S.B. Shaklan, R. Belikov, N.J. Kasdin, Fabrication and characteristics of free-standing shaped pupil masks for tpf-coronagraph, in: Proceedings of the SPIE Astronomical Telescopes and Instrumentation, number 130 in 6265, 2006.
[10] D.P. Ceperley, A.R. Neureuther, M.D. Lieber, N.J. Kasdin, Stray-light sources from pupil mask edges and mitigation techniques for the tpf coronagraph, in: Proceedings of the SPIE Astronomical Telescopes and Instrumentation, number 60 in 6271, 2006.
[11] M.D. Lieber, A.R. Neurether, D.P. Ceperley, N.J. Kasdin, Evaluating the end-to-end performance of tpf-c with vector propagation models and wavefront control, in: Proceedings of the SPIE Conference on Optics and Photonics, number 20 in 5905, 2005.
[12] R. Belikov, A. Give'on, M.A. Carr, J.T. Trauger, F. Shi, K. Balasubramanian, A.C. Kuhnert, N.J. Kasdin, Toward 10^{10} contrast for terrestrial exoplanet detection: demonstration of extreme wavefront correction in a shaped-pupil coronagraph, in: Proceedings of the SPIE Astronomical Telescopes and Instrumentation, number 42 in 6265, 2006.
[13] J.T. Trauger, C. Burrows, B. Gordon, J.J. Green, A.E. Lowman, D. Moody, A.F. Niessner, F. Shi, D. Wilson, Coronagraph contrast demonstration with the high-contrast imaging testbed, in: Proceedings of SPIE Conference on Astronomical Telescopes and Instrumentation, number 1330-1336 in 5487, 2004.